DOI 10.36146/2026_01_44

Correlation between starter block geometry, crystal orientation, and creep rupture life in CMSX-4 single crystals

A. Jadidi, S. M. Abbasi, M. Seifollahi

This study investigates the effect of starter-block geometry, expressed by the diameter-to-height (D/H) ratio, on crystallographic orientation and creep rupture behavior of CMSX-4 single-crystal superalloys. Directional solidification was performed using the vertical Bridgman process at a constant withdrawal rate of 9 mm/min with starter blocks of D/H = 0.3, 0.5, and 0.7. The resulting misorientations from the preferred [001] direction were 6.3°, 21.7°, and 3.3°, respectively, indicating that crystallographic orientation does not vary monotonically with the D/H ratio. Complementary thermal simulations performed using ProCAST showed distinct transitions in solidification-front stability across the selected geometries, providing a physical explanation for the non-monotonic trend in misorientation.

Creep rupture life at 850 °C and 560 MPa was measured to be 97.8, 24.6, and 122.6 h for the three samples, demonstrating a strong inverse dependence of creep resistance on crystallographic deviation. Fractographic analyses revealed more severe interdendritic cavitation and porosity coalescence in the highly misoriented specimens, confirming cavitation-dominated failure. In the best-oriented sample (3.3°), EDS measurements near creep cavities showed Re depletion in the γ/γ′ matrix and the formation of Re-rich secondary precipitates, indicating diffusion-driven segregation and stress-assisted precipitation during creep.

Overall, the results show that crystallographic alignment, solidification-front stability, and porosity control are jointly critical for optimizing the high-temperature creep performance of CMSX-4 single crystals.

KEYWORDS: CMSX-4, SINGLE CRYSTAL SUPERALLOY, STARTER BLOCK GEOMETRY, CREEP RUPTURE LIFE, CRYSTALLOGRAPHIC ORIENTATION;

INTRODUCTION

The CMSX-4 single-crystal superalloy was introduced by Cannon Muskegon Foundry in 1991, and by 2004, over 2200 tons of this material had been produced [1]. Its strengthening mechanism is based on solid-solution strengthening by Cr, W, and Ta, and precipitation hardening by Al and Ti through the formation of the γ′ phase [1,2]. Partial substitution of W with Ta was implemented to enhance castability, increase the γ′ volume fraction (up to 68%), improve γ′ strength, oxidation resistance, and coating stability. Among nickel-based superalloys, CMSX-4 exhibits a favorable balance of mechanical performance, largely due to its high-volume fraction of coherent γ′ precipitates with a $(Ni)_3(Al,Ti)$ composition formed during heat treatment [3,4].

In single-crystal casting, key process variables such as

A. Jadidi, S. M. Abbasi,
M. Seifollahi

Faculty of Materials and Manufacturing Technologies,
Malek Ashtar University of Technology, Iran

mold withdrawal rate, heat transfer rate, and the initial seed position must be carefully controlled to minimize deviation from the [001] crystallographic orientation. Because the matrix phase of nickel-based superalloys has an FCC structure, fewer slip systems are activated when loading is applied along [001]; thus, this direction offers superior creep resistance [5–7]. Misorientation angles below 12–15° are generally acceptable, and the largest deviations typically occur in the upper regions of the casting, farthest from the chill plate [8–10].

The role of early grain selection is crucial in determining the final crystal orientation. Yang et al. [11] reported that alignment between the heat-flow direction and dendrite growth is essential for suppressing stray grains. Carter et al. [12] identified optimal starter-block dimensions for CMSX-4 (D/H = 0.8), while Wang et al. [13] observed lower misorientation when the D/H ratio is close to 0.5. Sadeghi et al. [14] likewise recommended D/H values below 0.6 to stabilize competitive grain growth.

Recent studies have further highlighted that the efficiency of grain selection is highly sensitive to the geometrical characteristics of the selector and starter block. Variations in selector wire diameter, take-off angle, and pitch length can significantly alter the local thermal field, modify dendrite blocking efficiency, and influence stray-grain formation, particularly through changes in local undercooling [15]. Phase-field simulations of CMSX-4 have also demonstrated that solidification is accompanied by strong multicomponent segregation: γ′-stabilizing elements such as Al, Ti, and Ta enrich the interdendritic liquid, whereas refractory γ-stabilizing elements (Re, W, Co) are depleted. These segregation patterns control the formation of eutectic colonies and can influence homogenization behavior and creep response [16].

Given that single-crystal superalloys typically operate above 1000 °C, creep resistance is a critical property. Primary creep in CMSX-4 occurs through the <112>{111} slip system, and alignment with [001] significantly improves rupture life [7]. Orientation strongly affects creep behavior: samples aligned with [110] show shorter rupture lives than those near [100] [17], and even after heat treatment, crystals closer to [011] remain less creep-resistant [3]. Stress redistribution due to orientation has also been shown to play a decisive role in turbine-blade performance [18,19].

Microstructural evolution during high-temperature deformation introduces additional complexity. It has been shown that refractory and γ′-stabilizing elements may segregate to regions of high dislocation density, where local chemical perturbations subsequently drive microstructural changes, damage accumulation, and cavity formation during creep [20]. Complementary creep studies indicate that the redistribution of refractory elements (Re, W, Mo) governs the local stability of γ/γ′ microstructures: enrichment in dendrite cores stabilizes dislocation networks, while chemical gradients promote the formation of secondary γ′ structures in mesh regions under high-temperature creep conditions [21].

Based on the above, differing views persist regarding the influence of starter-block geometry (particularly the diameter-to-height ratio) on crystallographic deviation. Competitive grain selection depends not only on nucleation events near the chill plate but also on how geometrical constraints shape the thermal gradient and dendrite competition. Furthermore, the final orientation is dictated by the grain that successfully propagates through the spiral selector, directly affecting high-temperature performance, including rupture life.

Therefore, the objective of this study is to establish a clear correlation between the starter-block diameter-to-height ratio and the resulting crystallographic orientation and creep rupture life of CMSX-4 single crystals, supported by fractographic analysis to elucidate the underlying failure mechanisms.

MATERIALS AND METHODS

The chemical composition of the CMSX-4 ingot used for single-crystal casting is listed in table 1. The alloy contains key strengthening elements such as Al and Ti (γ′ formers), Cr and Co (solid-solution and stability elements), and refractory elements including Ta, W, and Re, with Ni as the balance.

Tab.1 - Chemical composition of the CMSX-4 ingot used in this study.

Element	Al	Ti	Cr	Co	Hf	Ta	W	Re	Mo	Ni
wt.%	5.6	0.98	6.5	9.59	0.097	6.6	6.6	3.05	0.7	Bal.

Trace concentrations of interstitial impurities (O, N, H, S, C) in the refined melt are presented in table 2. The low levels of these elements indicate that the starting material possessed sufficient purity for high-quality directional solidification.

Tab.2 - Minor element concentrations in the refined ingot.

Element	O	N	H	S	C
Amount	13.5 ppm	5.1 ppm	2 ppm	0.002 wt.%	<0.001 wt.%

The 3D model of the casting cluster (including the starter block, a 3D spiral grain selector, a central cylindrical rod, and supporting features) was designed using Rhinoceros 8 software. A schematic of the cluster system is shown in Figure 1. In the grain-selector design, fixed parameters were maintained: a starting angle of 30°, selector diameter of 3 mm, and a rotation angle of 180°. The starter-block height was held constant at 30 mm, while the diameter was varied to obtain diameter-to-height (D/H) ratios of 0.3, 0.5, and 0.7 (corresponding to diameters of 9, 15, and 21 mm).

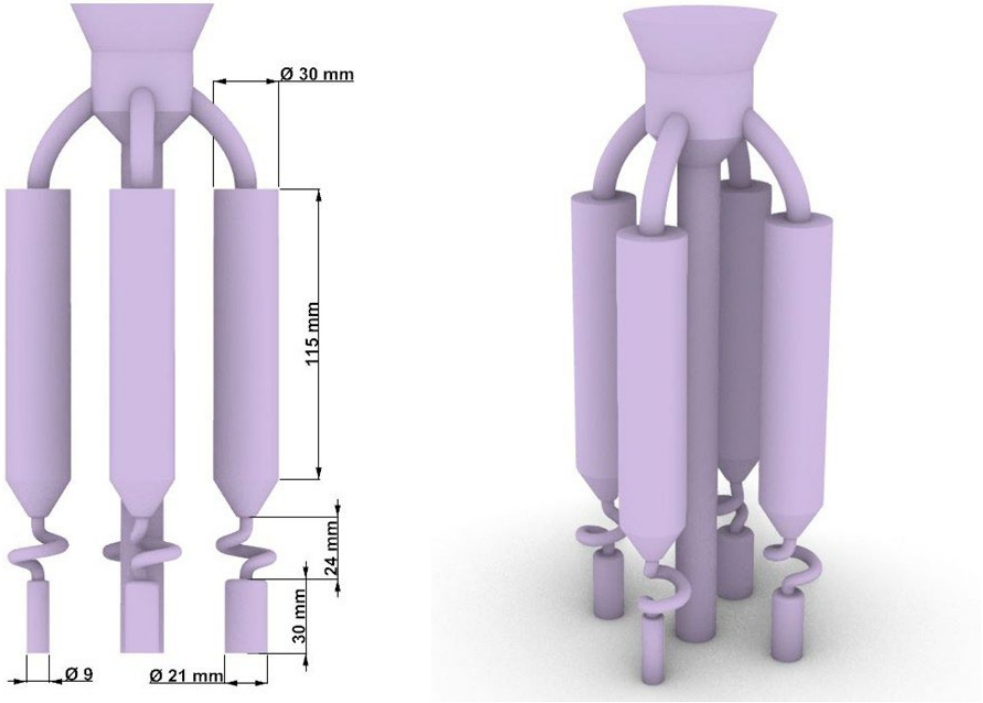

Fig.1 - Schematic of the cluster system designed for the fabrication of ceramic molds used in this study.

After fabrication of the wax components, they were assembled and coated with multiple ceramic slurry layers to form the shell mold. Directional solidification was conducted in an HRS-type vertical Bridgman furnace equipped with a graphite baffle. The pouring and hot-zone temperatures were each set to 1500 °C. A constant mold withdrawal rate of 9 mm/min was used for all castings.

After solidification, the ceramic mold was removed, and the castings were sectioned using a wire-cut electrical discharge machine. Samples were ground, polished, and etched using Marble's reagent (10 g $CuSO_4 \cdot 5H_2O$, 50 mL HCl, 50 mL distilled water) for 45 s at room temperature.

Optical microstructural examinations were performed using an OLYMPUS DP25 microscope. Quantitative and qualitative analyses of elemental segregation were conducted using a TESCAN MIRA3 field-emission SEM (FE-SEM) equipped with an energy-dispersive spectroscopy (EDS) detector.

Secondary dendrite arm spacing (λ_2) was measured from longitudinal etched sections using the D-method of Vandersluis and Ravindran [22]. ImageJ software was used to measure arm-to-arm distances; each λ_2 value represents the average of ten measurements taken from five micrographs. Primary dendrite arm spacing (λ_1) was obtained from cross-sectional etched images using the area-counting method expressed as:

$$\lambda_1 = \sqrt{\frac{A}{n}} \quad (1)$$

where (A) is the analyzed area (μm^2) and (n) is the number of primary dendrite cores within that area [23].

Crystallographic orientation deviation from the [001] direction was measured using an X-ray crystal-orientation analyzer (Asenware Ltd.). All samples underwent the standard CMSX-4 heat-treatment schedule prior to creep rupture testing. The specimen geometry and the testing setup (Azar Furnace) are illustrated in figure 2.

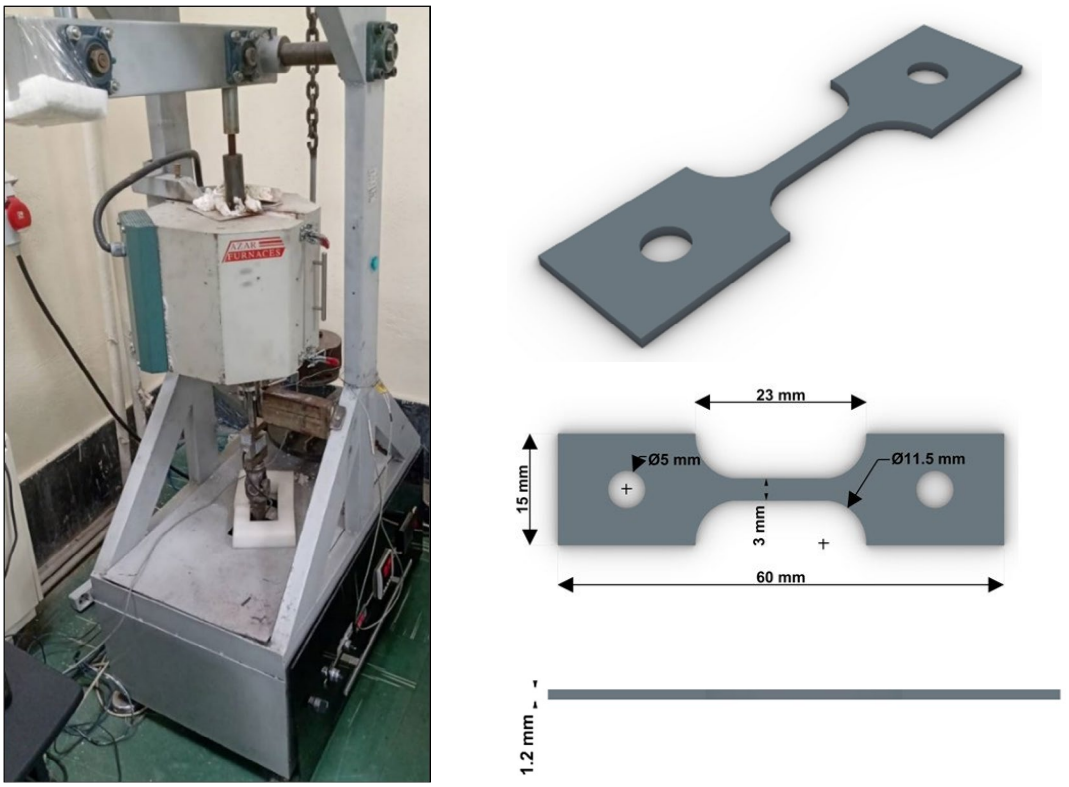

Fig.2 - Schematic of the flat specimen used for rupture life testing, shown alongside the creep testing apparatus employed in this study.

Finite-element thermal simulations were performed using ProCAST to evaluate the solidification behavior within starter blocks of different D/H ratios. The built-in CMSX-4 alloy database was used, and all thermophysical properties (thermal conductivity, density, specific heat, latent heat, and solidus/liquidus temperatures) were taken directly from the software's material library.

The thermal boundary conditions were defined to replicate the experimental directional solidification process. The inner surface of the heating zone was set to 1500 °C, while the chill plate temperature was fixed at 20 °C. Surface emissivities were assigned as follows: 0.85 for graphite components, 0.80 for the ceramic mold, 0.50 for the inner surface of the cold zone, and 0.40 for the thermal insulation layer.

Convective and contact heat-transfer coefficients were applied according to standard Bridgman solidification practice. The heat-transfer coefficient between the cooling medium and the mold was set to 20 W m^{-2} K^{-1}, and that between the cooling medium and water to 5000 W m^{-2} K^{-1}. The interfacial heat-transfer coefficient between the casting and chill plate was temperature-dependent, varying from 196 W m^{-2} K^{-1} at 1473 K to 750 W m^{-2} K^{-1} at 1773 K. Similarly, the casting–mold interface coefficient was defined as temperature-dependent, increasing from 50 W m^{-2} K^{-1} at 773 K to 750 W m^{-2} K^{-1} at 1773 K.

The entire casting (including the starter block, spiral grain selector, and cylindrical casting region) was meshed with a uniform 1 mm element size. Coarse meshes of 10 mm were used for the insulation layer and furnace walls to reduce computational cost. The ceramic mold thickness was set to 8 mm, consistent with the experimental fabrication.

RESULTS AND DISCUSSION

Figure 3 shows the as-cast single-crystal specimens together with the grain-selection system after separation from the central runner. The starter blocks used in these castings were produced with diameter-to-height (D/H) ratios of 0.3, 0.5, and 0.7, enabling a direct comparison of how starter-block geometry influences grain competition during directional solidification.

Fig.3 - Single crystal castings with the grain selection system after separation from the central runner. The samples correspond to starter blocks with diameter-to-height (D/H) ratios of 0.3 (left), 0.5 (center), and 0.7 (right).

According to post-casting Laue back-reflection measurements, supported by cross-sectional examination near the upper region of the grain selector, all three specimens were confirmed to be single crystals. The crystallographic orientation deviations from the preferred [001] growth direction were subsequently quantified using X-ray diffraction analysis, as presented in figure 4.

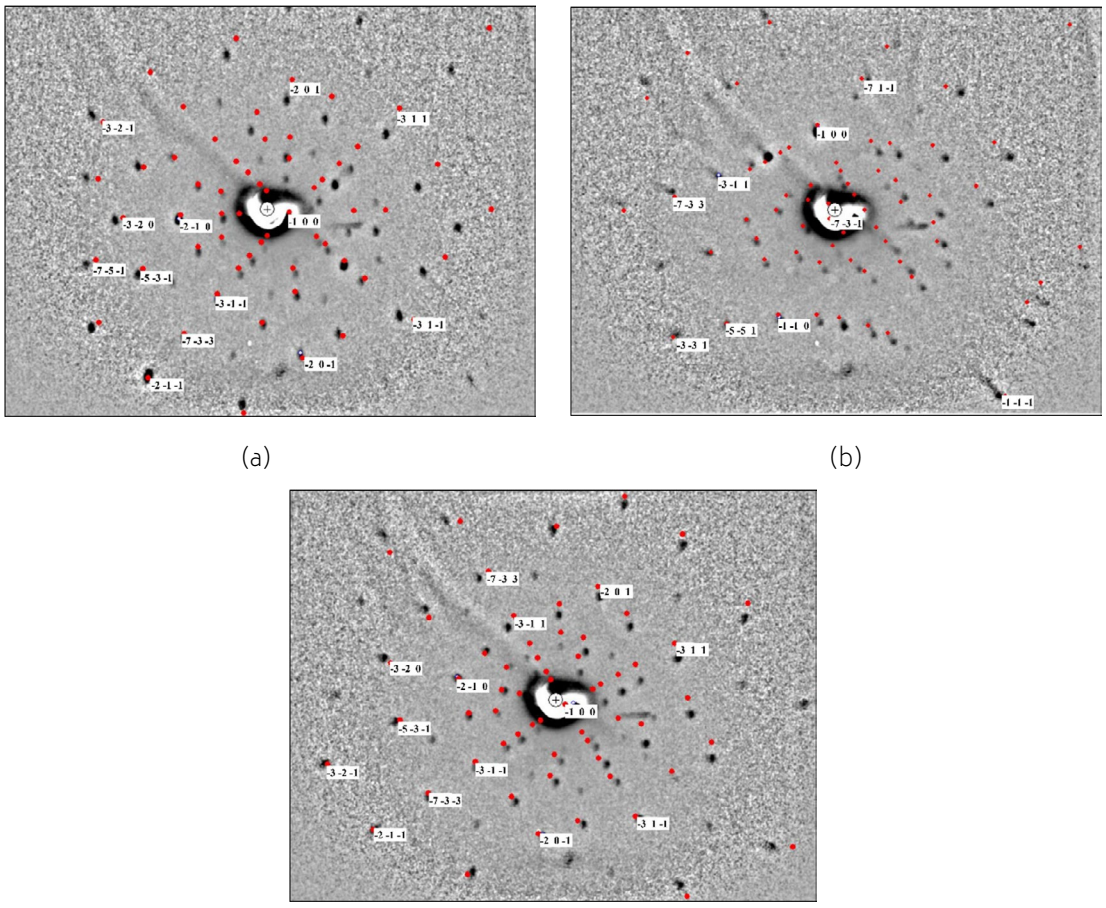

Fig.4- X-ray diffraction patterns obtained from Laue tests for single crystal samples cast with starter block diameter-to-height (D/H) ratios of (a) 0.3, (b) 0.5, and (c) 0.7.

Based on the X-ray diffraction results shown in figure 4, the crystallographic deviations from the preferred [001] orientation were determined to be 6.3°, 21.7°, and 3.3° for the single-crystal samples produced with starter block D/H ratios of 0.3, 0.5, and 0.7, respectively. The absence of a monotonic or linear trend between the D/H ratio and the resulting deviation angle indicates that crystallographic alignment is not governed solely by the geometric ratio of the starter block. Instead, these results suggest a more complex interaction among local thermal gradients, the number of nucleated grains at the chill plate, and competitive dendrite growth within the restricted starter-block volume. Small variations in initial nucleation density or in the orientation of early surviving grains can dominate the final selected grain, leading to non-systematic orientation outcomes even when geometric parameters appear well controlled.

In addition to these factors, it should be noted that the selected D/H ratios (0.3, 0.5, and 0.7) represent relatively large incremental changes ($\Delta = 0.2$), which may obscure the gradual evolution of the solidification mechanism inside the starter block. At a D/H ratio of 0.3, the reduced cross-section limits heat extraction through the starter block walls, resulting in a noticeably lower thermal gradient and a slower advancement of the solidification front. Under such conditions, thermal filtering becomes less effective and the solid–liquid interface remains insufficiently constrained, allowing misoriented grains to survive longer during competitive growth. This environment increases the likelihood of stray-grain formation. As the D/H ratio increases, heat extraction becomes more efficient, the thermal gradient strengthens, and the solidification front advances more steadily. These improvements enhance competitive grain selection and promote the

suppression of unfavorably oriented grains. This gradual shift in interface behavior across the examined D/H ratios provides a plausible physical explanation for the observed differences in stray-grain formation and clarifies why the final [001] deviation does not follow a linear or monotonic trend with D/H. These experimentally inferred thermal behaviors were further verified through numerical simulation.

Finite-element thermal simulations (ProCAST) further clarified why the experimentally observed misorientations did not follow a monotonic trend with starter-block geometry. As also reflected in the longitudinal-section observations of figure 5, the isothermal-velocity maps demonstrated that at D/H = 0.3 the solidification front exhibits relatively high isotherm velocities and an unstable progression, indicating weak thermal gradients and inefficient heat extraction. Under these conditions, thermal filtering inside the starter block becomes ineffective, enabling the survival of misoriented grains. Increasing the ratio from 0.3 to 0.5 reduced isotherm velocity but did not fully stabilize the interface, suggesting that this interval corresponds to a transition regime where the dominant solidification mechanism remains partially unstable. In contrast, the change from D/H = 0.5 to 0.7 resulted in a marked drop in isotherm velocity and the development of a flat, well-anchored solidification front with significantly stronger thermal gradients; consistent with the absence of stray grains in figure 5 and with the minimal [001] deviation measured at D/H = 0.7. These simulation-supported trends explain why small geometric changes do not produce proportional orientation changes and why the 0.5 sample shows the largest misorientation despite having an intermediate geometry.

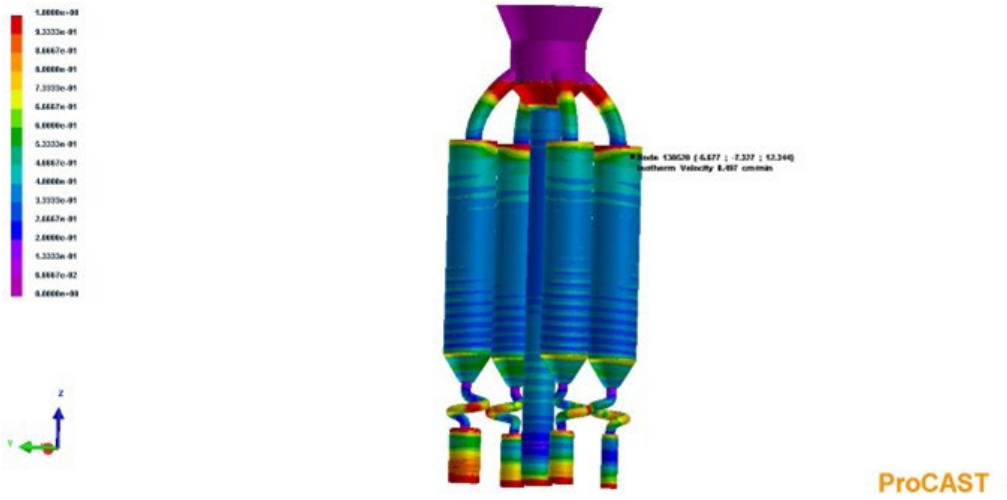

Fig.5 - Isotherm-velocity contours from ProCAST simulations for starter blocks with different D/H ratios, corresponding to steady-state conditions after initial thermal equilibration.

Recent numerical analyses of grain selectors have shown that small geometrical modifications can significantly alter the local thermal field and the degree of undercooling, thereby affecting competitive dendrite growth and the stability of grain selection. These observations are consistent with the trends observed in the present ProCAST simulations, where changes in the starter-block geometry modified the isotherm velocity and interface stability [15].

The longitudinal sections presented in figure 6 further illustrate the influence of starter-block geometry on grain selection. Stray grains were observed in the castings with D/H ratios of 0.3 and 0.5, predominantly located in the upper region of the starter block and adjacent selector zone. These misoriented grains likely arise from insufficient thermal filtering and reduced competitive growth efficiency when the starter block does not impose enough lateral constraint on early dendrite growth. This interpretation is consistent with earlier findings in the literature: Yang et al. [11] demonstrated that inadequate thermal alignment within the starter block facilitates the survival of misoriented grains, while Carter et al. [12] and Wang et al. [13] showed that the efficiency of thermal filtering and competitive grain selection

is strongly governed by starter-block geometry, with suboptimal D/H ratios increasing the likelihood of stray-grain formation. Sadeghi et al. [14] further confirmed that variations in the D/H ratio directly influence the stability of the solidification front and the probability of stray-grain generation. In contrast to the D/H = 0.3 and 0.5 specimens, the casting produced with a D/H ratio of 0.7 exhibited no detectable stray grains in the examined section, indicating a more effective suppression of competitive grains and stronger selection of a dominant dendrite.

It should be noted, however, that figure 6 represents a single longitudinal plane from each casting. Given the inherently three-dimensional nature of dendritic growth and competitive grain selection, the spatial distribution and volume fraction of stray grains may vary in other sections of the same specimen. Nonetheless, the consistent presence or absence of stray grains across both D/H = 0.3 and 0.5 samples provides strong qualitative evidence that starter-block geometry influences grain-selection stability, even if it does not uniquely determine the final [001] deviation angle.

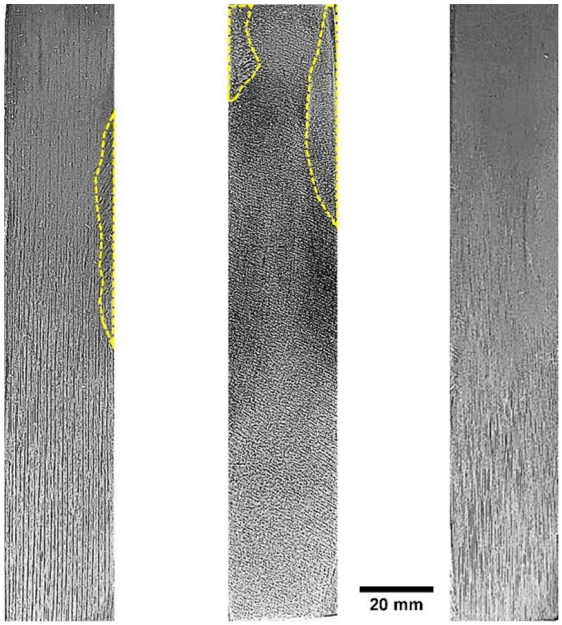

Fig.6- Macroscopic images of the longitudinal sections of single crystal castings after etching, corresponding to starter block diameter-to-height (D/H) ratios of (a) 0.3, (b) 0.5, and (c) 0.7. Stray grains are highlighted as dotted regions.

Figure 7 shows the cross-sectional microstructures of the single-crystal castings produced with different starter block D/H ratios. The contrast differences among the images (particularly the darker appearance in (b)) arise from variations in the local dendrite orientation relative to the [001] growth direction, which affects the way the etched surface reflects light. Tertiary dendrite arms are clearly visible in all samples and fill the interdendritic regions. These branches form once the primary dendrites exit the selector and enter the wider mold cavity, where sufficient lateral space is available for full dendritic development. In contrast, dendrite branching inside the starter block is noticeably restricted due to the limited cross-sectional area and intense competitive growth among neighboring grains, which suppresses the formation of secondary and tertiary arms during the early stages of solidification.

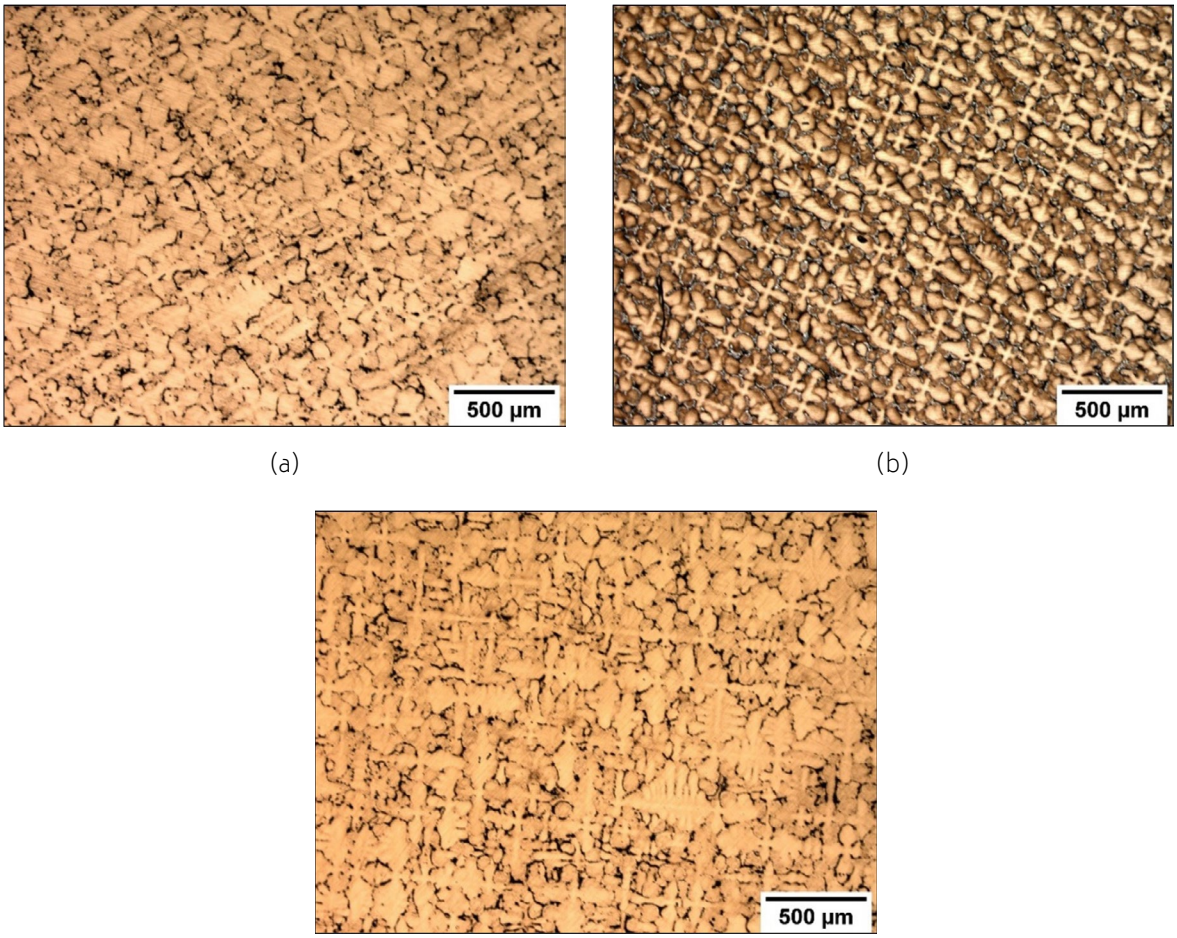

Fig.7- Optical micrographs of the cross-sectional areas of as-cast single crystal samples after etching, corresponding to starter block diameter-to-height (D/H) ratios of (a) 0.3, (b) 0.5, and (c) 0.7.

The average primary dendrite arm spacing (λ_1) was calculated using Equation 1 based on dendrite core counting in the cross-sectional micrographs. The measured λ_1 values for the samples with starter block D/H ratios of 0.3, 0.5, and 0.7 were 226.4 µm, 232.4 µm, and 241.6 µm, respectively. Although a slight increasing trend is observed, the differences fall within the typical measurement uncertainty for this method and are therefore not considered significant. This limited variation is expected, as λ_1 is primarily governed by the local thermal gradient and solidification rate in the mold cavity; parameters that remained nearly constant across all castings due to the identical withdrawal rate and furnace conditions used in the process.

The average secondary dendrite arm spacing (λ_2) for the samples with starter block diameter-to-height (D/H) ratios of 0.3, 0.5, and 0.7 was measured to be 41.3 µm, 36.7 µm, and 39.3 µm, respectively. Although λ_2 shows a slight decrease from D/H = 0.3 to 0.5 followed by a modest increase at D/H = 0.7, these fluctuations lie within the expected range of experimental and image-based measurement uncertainty. Consequently, no systematic or physically meaningful correlation between λ_2 and the starter-block geometry can be established. This behavior is consistent with the fact that λ_2 is predominantly controlled by the local cooling rate in the selector exit and mold cavity; parameters that remained essentially unchanged because all castings were produced under identical furnace conditions and a constant withdrawal rate. The longitudinal micrographs used for λ_2 measurements are not reproduced here to avoid redundancy with previous studies employing the same methodology.

This lack of sensitivity of λ_1 and λ_2 to the starter-block D/H ratio is consistent with previous findings by Carter et al. [12], Wang et al. [13], and Sadeghi et al. [14], who reported that dendrite arm spacings are primarily controlled by the local cooling rate and thermal gradient in the mold cavity, and are largely unaffected by variations in starter-block geometry when the withdrawal rate and furnace conditions remain constant.

Figure 8 illustrates the rupture life of the heat-treated single-crystal samples tested at 850 °C and 560 MPa, plotted as a function of their deviation from the preferred [001] crystallographic orientation. A clear inverse relationship is observed: increasing the deviation from 3.3° to 6.3° reduces the rupture life from 123 to 98 h (~20%), and a further increase to 21.7° results in a drastic drop to 25 h, representing an ~80% reduction relative to the best-aligned specimen. This systematic and strong degradation trend reflects the strong sensitivity of CMSX-4 to crystallographic misalignment, as deviation from the <001> axis increases the resolved shear stress on critical slip and climb systems, promotes earlier γ' shearing or rafting in unfavorable directions, and accelerates cavity nucleation and coalescence during creep. Thus, even modest deviations from the ideal growth direction have a pronounced detrimental effect on creep rupture life.

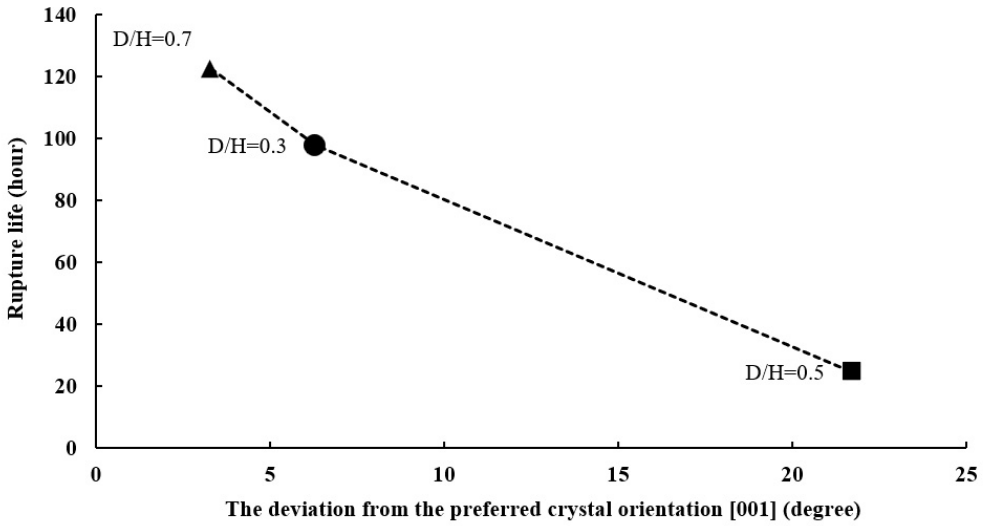

Fig.8 - Rupture life of samples prepared from single crystal castings with different diameter-to-height (D/H) ratios, as a function of deviation from the preferred [001] crystallographic orientation. All samples were tested at 850 °C and 560 MPa after standard heat treatment.

This strong inverse dependence between misorientation and rupture life is consistent with previous reports showing that even moderate deviations from the <001> axis increase the activation of non-preferred slip systems and accelerate creep damage in CMSX-4 and other nickel-based single crystals [3,7,17–19]. However, the magnitude of the reduction observed in this study is more pronounced, which can be attributed to the combined effects of crystallographic misalignment and casting-induced porosity under the relatively high withdrawal rate used.

Literature reports for CMSX-4 show that single crystals tested at 850 °C and 560 MPa with near-ideal [001] alignment typically exhibit rupture lives of 150–170 h [24]. In contrast, the highest rupture life obtained in the present study was 123 h for the specimen with only 3.3° misorientation. This reduction cannot be explained solely by the slight orientation deviation; instead, it is primarily associated with the relatively high mold withdrawal rate used during directional solidification (9 mm/min). Such a withdrawal rate decreases the local thermal gradient and increases solidification velocity, conditions known to promote interdendritic porosity formation. The residual pores were not fully eliminated during the standard heat-treatment cycle and subsequently acted as preferential nucleation sites for creep cavitation. Their presence

accelerated cavity growth and damage accumulation, thereby reducing the rupture life even in the best-oriented sample.

Fractographic examination of all tested specimens revealed the presence of interdendritic cavities, indicating that residual casting porosity played an active role in creep damage evolution. These cavities frequently showed signs of symmetric damage initiation on opposing faces, a characteristic feature of cavitation-controlled rupture in single-crystal superalloys. Such morphology suggests that cavity nucleation occurred preferentially at pre-existing pores, followed by stress-assisted growth and coalescence during creep. Figure 9 illustrates a representative example from the sample with a 21.7° deviation, where a pronounced double-lobed cavity structure is clearly visible near the fracture surface, consistent with advanced cavitation and localized stress concentration.

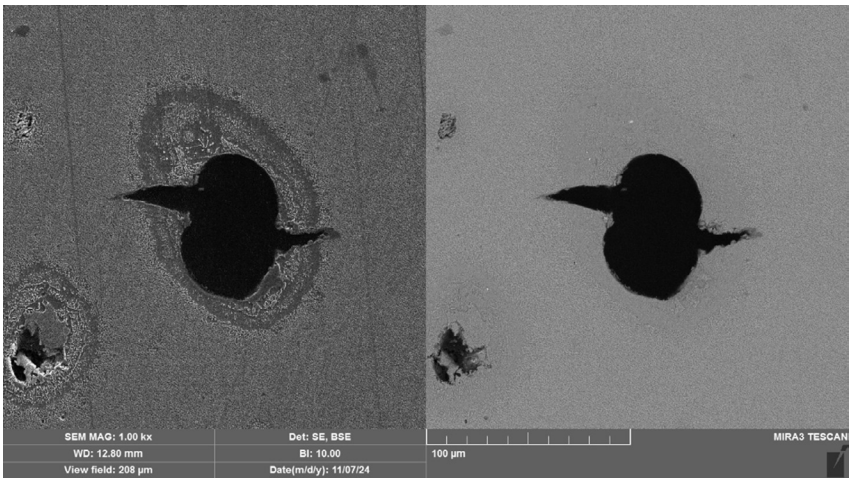

Fig.9 - SEM image of an interdendritic cavity near the fracture region in the sample with 21.7° deviation from [001].

To further interpret the results presented in figure 8 (where a pronounced reduction in rupture life was observed with increasing deviation from the [001] crystallographic orientation) a comparative fractographic analysis was conducted. The objective of this analysis was to identify the underlying microstructural damage mechanisms responsible for the variation in creep performance among the samples. By examining the fracture surfaces, it was possible to assess the role of casting-induced porosity, cavitation behavior, and deformation-induced microstructural features, thereby establishing a direct link between crystallographic misalignment and the dominant creep damage pathways.

Figure 10 presents SEM images of the fracture surfaces of the single-crystal samples produced with starter-block D/H ratios of 0.3, 0.5, and 0.7. All micrographs were captured at the same magnification (70×) to enable a direct comparison of cavity morphology and failure characteristics. The specimen with the lowest deviation from the [001] direction (3.3°, D/H = 0.7) exhibits a relatively uniform and fine-scale fracture surface, with limited evidence of cavity nucleation or coalescence. In contrast, the sample with the highest misorientation (21.7°, D/H = 0.5) shows a markedly rougher fracture surface containing numerous irregular and coalesced cavities, consistent with the progression of severe creep damage prior to rupture. The intermediate specimen (6.3°, D/H = 0.3) displays fracture features between these two extremes, presenting a mixture of isolated cavities and partially coalesced voids. This systematic transition in fracture morphology reinforces the observed trend in rupture life, indicating that increasing crystallographic deviation promotes more aggressive cavitation-driven damage accumulation.

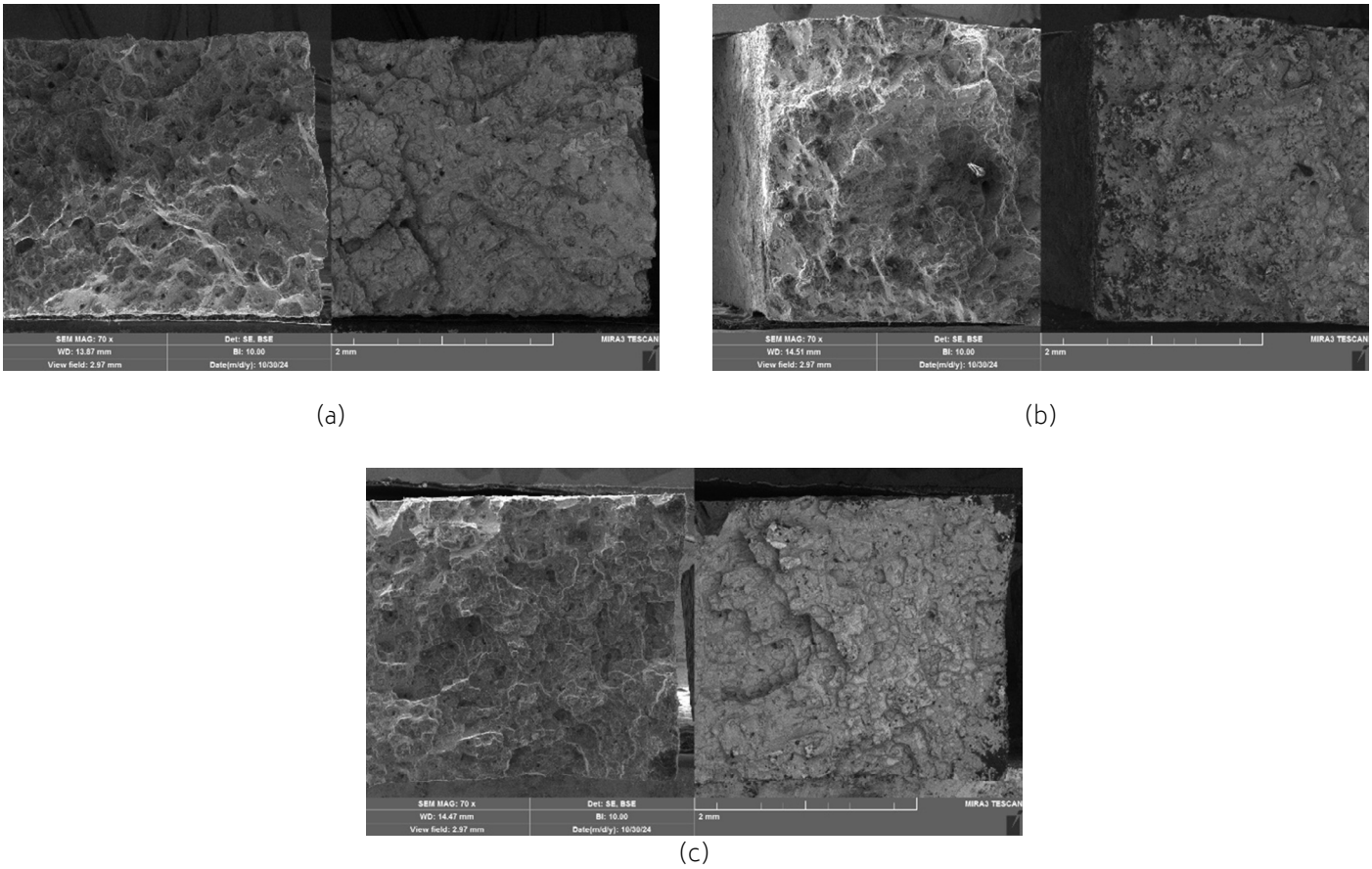

Fig.10 - SEM images of the fracture region for single crystal samples with different starter block diameter-to-height ratios: (a) 0.3, (b) 0.5, (c) 0.7.

The higher-magnification images presented in figure 11 provide further confirmation that cavitation-mediated damage is the dominant creep-rupture mechanism in all samples. Interdendritic cavities, microvoids, and early-stage coalescence features are visible throughout the fracture surfaces, consistent with creep deformation occurring preferentially along interdendritic regions. However, clear differences emerge in the extent and morphology of these damage features. The specimen with the largest crystallographic deviation (21.7°) exhibits extensive cavity coalescence, larger void clusters, and more irregular cavity networks, indicating accelerated damage accumulation and reduced resistance to creep deformation. In contrast, the samples with lower deviations (including the 3.3° specimen) show smaller, more isolated cavities with limited linkage, reflecting a slower progression of void growth. This systematic variation in cavity morphology strongly supports the correlation between increasing misorientation from the [001] axis and the severity of cavitation-driven rupture.

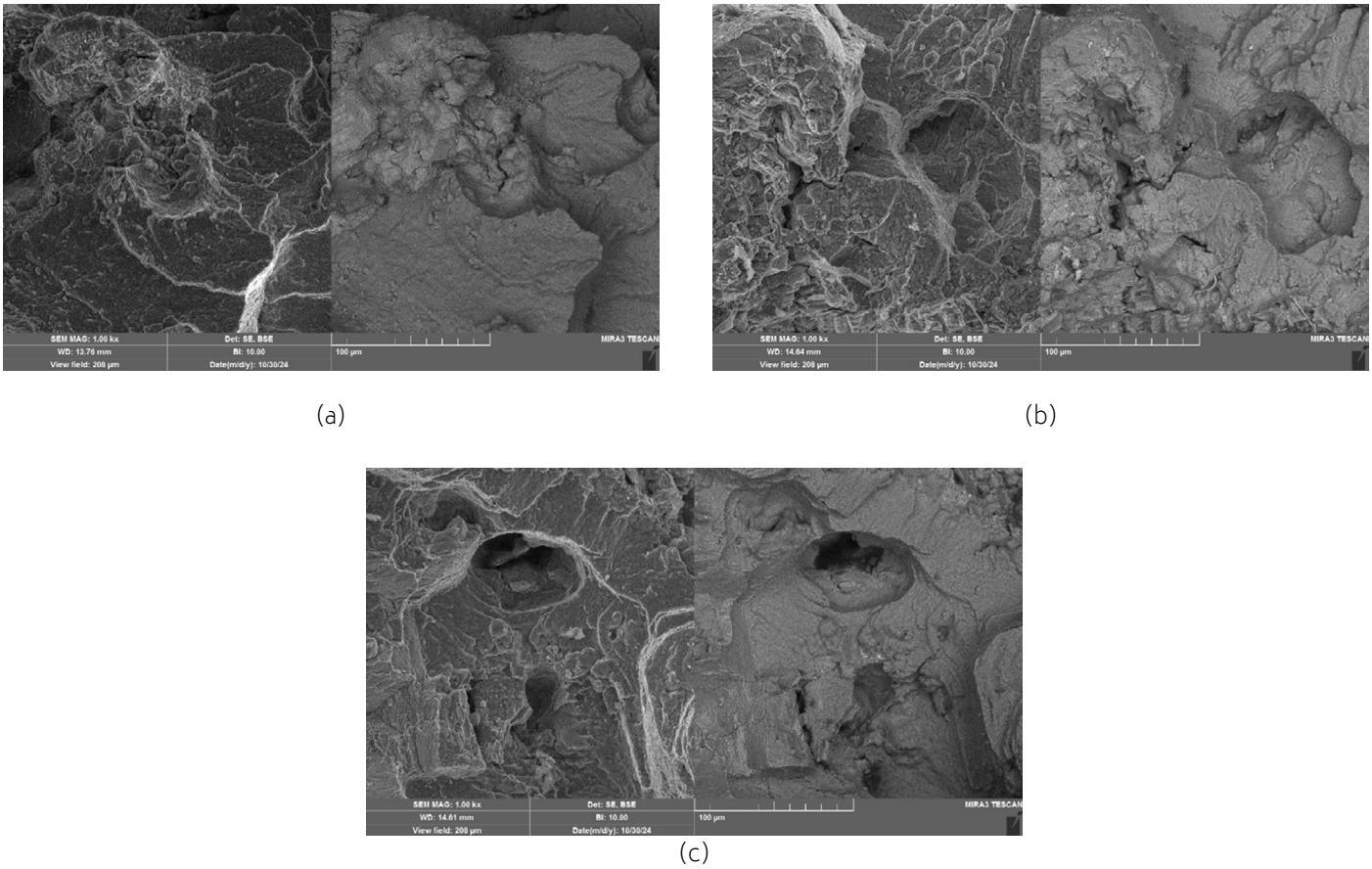

Fig.11 - High-magnification SEM images (1000×) of the fracture surfaces of single crystal samples with different starter block diameter-to-height ratios: (a) 0.3, (b) 0.5, (c) 0.7.

In summary, the fracture-surface analysis confirms that cavitation is the dominant mechanism governing creep rupture in CMSX-4 single crystals under the present testing conditions. Although all specimens exhibited interdendritic cavities, clear differences in cavity size, morphology, and degree of coalescence were observed as a function of crystallographic deviation from the [001] orientation. Samples with larger misorientations displayed more irregular and extensively coalesced cavities, reflecting enhanced local stress concentrations and accelerated void growth. Conversely, specimens with lower deviation exhibited smaller, more isolated cavities, indicating a slower progression of creep damage. These fractographic trends are fully consistent with the rupture-life results, demonstrating that misorientation increases the activation of non-preferred slip systems, thereby amplifying the detrimental effects of casting-induced porosity. Collectively, the findings show that both accurate crystallographic alignment and effective porosity control are essential for achieving optimal creep performance in single-crystal superalloys.

To further assess the microstructural integrity of the best-performing specimen, SEM imaging was carried out on the fracture region of the single-crystal sample with the smallest deviation from the [001] crystallographic direction (3.3°). Figure 12 presents a representative backscattered-electron micrograph in which two locations were selected for EDS analysis.

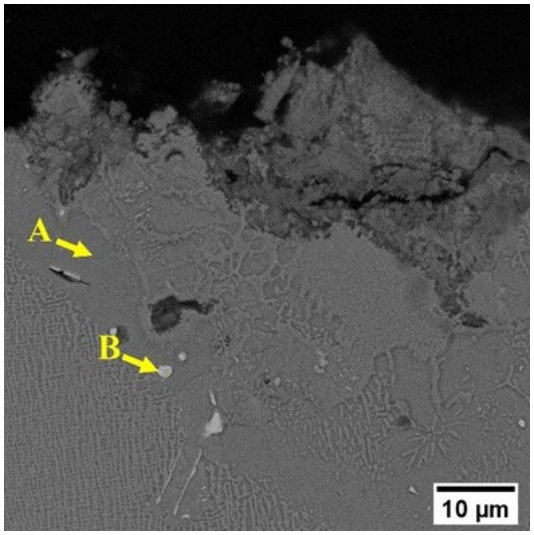

Fig.12 - SEM image of the fracture region in the 3.3° deviation sample, showing the locations of points A (matrix adjacent to cavity) and B (precipitate-like region).

The elemental compositions measured at the two analyzed locations are summarized in figure 13. Point A (situated adjacent to the halo-like region surrounding a creep cavity) exhibits elevated Al and Ti contents, reflecting the γ′-rich matrix where local redistribution has occurred during creep. Point B, taken from the bright precipitate-like feature visible in the backscattered image, shows pronounced enrichment in heavy refractory elements, particularly Re. This compositional contrast confirms that stress-assisted, Re-rich secondary precipitates form in the vicinity of creep damage, accompanied by measurable depletion of refractory elements in the surrounding matrix. The simultaneous occurrence of matrix depletion at Point A and heavy-element enrichment at Point B provides strong evidence for diffusion-driven segregation processes that promote cavity nucleation and accelerate damage evolution, even in the sample with near-ideal crystallographic orientation.

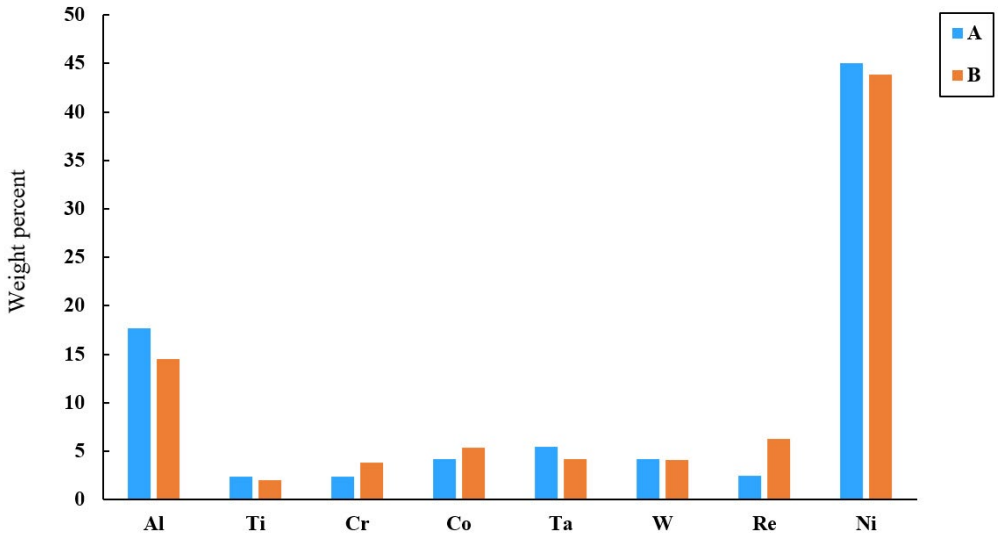

Fig.13 - Weight percent of selected elements at points A (adjacent to cavity) and B (Re-rich precipitate) in the fractured region of the 3.3° deviation sample.

Overall, these results demonstrate that elemental segregation and the formation of Re-rich secondary precipitates occur even in the single crystal with the smallest crystallographic deviation. The pronounced enrichment of Re and other heavy refractory elements within stress-assisted precipitates, together with their measurable depletion in the adjacent γ/γ' matrix, reflects an active diffusion-controlled redistribution during creep. This localized chemical imbalance reduces matrix stability and facilitates cavity nucleation and growth. Consequently, the findings show that accurate crystallographic alignment (while beneficial) cannot fully compensate for the detrimental effects of diffusion-induced segregation and residual porosity on the creep performance of CMSX-4 single crystals.

Although the formation of Re-rich secondary phases and their direct association with cavity nucleation have not been explicitly reported in the cited literature, the observed diffusion-controlled segregation is consistent with previously described creep-damage mechanisms in CMSX-4 and related single-crystal alloys [3,7,17–19], where local stress concentrations and refractory-element redistribution contribute to microstructural degradation during high-temperature deformation.

CONCLUSION

CMSX-4 single crystals were directionally solidified using starter-block D/H ratios of 0.3, 0.5, and 0.7, resulting in misorientations of 6.3°, 21.7°, and 3.3°, respectively, with no monotonic dependence on block geometry. ProCAST thermal simulations demonstrated that the 0.3→0.5 interval corresponds to an unstable solidification regime with high isotherm velocities, whereas the transition to D/H = 0.7 produces a stable, well-anchored front, explaining the presence of stray grains at low ratios and the minimal deviation at 0.7. Creep rupture testing showed a strong inverse relationship between misorientation and creep resistance, with rupture life decreasing sharply as deviation from the [001] direction increased. Microstructural evaluations revealed only minor variations in λ_1 and λ_2, confirming that dendrite spacing was not a critical factor in the performance differences. Fractography and EDS analysis identified interdendritic porosity, cavity coalescence, and diffusion-driven segregation of refractory elements as the dominant contributors to damage evolution. Together, these results demonstrate that both crystallographic alignment and porosity control (governed by starter-block design and solidification stability) must be optimized to achieve superior creep performance in CMSX-4 single crystals.

REFERENCES

[1] K. Harris, J. B. Wahl, "Improved single crystal superalloys, CMSX-4 (SLS)[La+ Y] and CMSX-486," Superalloys, 2004, pp. 45-52. Doi:10.7449/2004/Superalloys_2004_45_52

[2] A. Basak, D. Suman, "Effect of heat treatment on the microstructures of CMSX-4® processed through scanning laser epitaxy (SLE)," International Solid Freeform Fabrication Symposium, University of Texas at Austin, 2017. https://api.semanticscholar.org/CorpusID:210920054

[3] K. Harris, G. L. Erickson, R. E. Schwer, "Directionally solidified and single-crystal superalloys," Metals Handbook, 1990, Vol. 1, pp. 995-1006.

[4] Z. Li, J. Xiong, Q. Xu, J. Li, B. Liu, "Deformation and recrystallization of single crystal nickel-based superalloys during investment casting," Journal of Materials Processing Technology, 2015, Vol. 217, pp. 1-12.

[5] C. T. Liu, X. M. Li, B. Wang, Z. M. Ren, J. Y. Zhang, "Effect of Simulation Conditions on Grain Selection during Solidification of Single Crystal Casting," Advanced Materials Research, Trans Tech Publications, 2011, Vol. 146, pp. 829-833.

[6] L. W. Jiang, S. S. Li, M. L. Wu, Y. F. Han, "Grain Competition Mechanism of a Ni3Al-based Single Crystal Superalloy IC6SX," Materials Science Forum, Trans Tech Publications, 2013, Vol. 747, pp. 797-803.

[7] D. W. MacLachlan, G. S. K. Gunturi, D. M. Knowles, "Modelling the uniaxial creep anisotropy of nickel base single crystal superalloys CMSX-4 and RR2000 at 1023 K using a slip system based finite element approach," Computational Materials Science, 2002, Vol. 25, pp. 129-141. https://doi.org/10.1016/S0927-0256(02)00257-4

[8] B. Chmiela, M. Sozańska, "Analysis of high angle boundaries in directionally solidified turbine blade made of CMSX-4® superalloy," IOP Conference Series: Materials Science and Engineering, 2011, Vol. 22, No. 1, p. 012008 Doi: 10.1088/1757-899X/22/1/012008

[9] A. Onyszko, "Gamma Prime Crystal Lattice Orientation of Turbine Blades of the Single Crystal Nickel Based CMSX-4 Superalloy," Solid State Phenomena, Trans Tech Publications, 2013, Vol. 203, pp. 169-172.

[10] M. H. Raza, A. Wasim, S. Hussain, M. Sajid, M. Jahanzaib, "Grain Selection and Crystal Orientation in Single-Crystal Casting: State of the Art," Crystal Research and Technology, 2019, Vol. 54, p. 1800177.
[11] X. Yang, D. Ness, P. D. Lee, N. D'Souza, "Simulation of stray grain formation during single crystal seed melt-back and initial withdrawal in the Ni-base superalloy CMSX4," Materials Science and Engineering: A, 2005, Vol. 413, pp. 571-577.
[12] P. Carter, D. C. Cox, C. A. Gandin, R. C. Reed, "Process modelling of grain selection during the solidification of single crystal superalloy castings," Materials Science and Engineering: A, 2000, Vol. 280, pp. 233-246.
[13] N. Wang, L. Liu, S. Gao, X. Zhao, T. Huang, J. Zhang, H. Fu, "Simulation of grain selection during single crystal casting of a Ni-base superalloy," Journal of Alloys and Compounds, 2014, Vol. 586, pp. 220-229.
[14] F. Sadeghi, A. Kermanpur, E. Norouzi, "Optimizing Grain Selection Design in the Single-Crystal Solidification of Ni-Based Superalloys", Crystal Research and Technology, 2018, Vol. 53, p. 1800108.
[15] X. Zhu, F. Wang, D. Ma, "A Study of Grain Selection in Two-Dimensional (2D) Grain Selectors during the Investment Casting of Single-Crystal Superalloy," Materials, 2023, Vol. 16(11), p. 4112.
[16] M. Uddagiri, O. Shchyglo, I. Steinbach, M. Tegeler, "Solidification of the Ni-based superalloy CMSX-4 simulated with full complexity in 3-dimensions," Progress in Additive Manufacturing, 2024, Vol. 9(4), pp. 1185-1196.
[17] Q. Z. Chen,D. M. Knowles, "Mechanism of <112>/3 slip initiation and anisotropy of γ' phase in CMSX-4 during creep at 750° C and 750 MPa," Materials Science and Engineering: A, 2003, Vol. 356(1-2), pp. 352-367.
[18] D. Dye, A. Ma & R. C. Reed, "Numerical modelling of creep deformation in a CMSX-4 single crystal superalloy turbine blade," Superalloys, 2008, Vol. 911, e919.
[19] Y. Liang, S. Li, C. Ai, Y. Han and S. Gong, "Effect of Mo content on microstructure and stress-rupture properties of a Ni-base single crystal superalloy," Progress in Natural Science: Materials International, 2016, Vol. 26, pp. 112-116.
[20] P. Kontis & T. M. Smith, "A Review on the Partitioning of Solutes Along Dislocations and Stacking Faults in Superalloys," Metallurgical and Materials Transactions: A, 2024, Vol. 55(12), pp. 4723-4741.
[21] W. Xia, X. Zhao, Q. Yue, L. Yue, J. Wang, Q. Ding, H. Bei, Z. Zhang, "Formative and controlled mechanisms of nano-sized γ' precipitates with local phase-transition within dislocation networks of nickel-based single crystal superalloys," Acta Materialia, 2021, Vol. 206, p. 116653.
[22] E. Vandersluis, C. Ravindran, "Comparison of measurement methods for secondary dendrite arm spacing," Metallography Microstructure and Analysis, 2017, 6(1), 89-94.
[23] S. Kostić, A. Golubović, A. Valčić, "Primary and secondary dendrite spacing of Ni-based superalloy single crystals," Journal of the Serbian Chemical Society, 2009, Vol. 74(1), pp. 61-69.
[24] R. C. Reed, "The superalloys: fundamentals and applications," Cambridge University Press, 2008.